nature physics

ARTICLES

https://doi.org/10.1038/s41567-018-0046-7

Human brain organoids on a chip reveal the physics of folding

Eyal Karzbrun[1], Aditya Kshirsagar[1], Sidney R. Cohen[2], Jacob H. Hanna[1] and Orly Reiner[1*]

Human brain wrinkling has been implicated in neurodevelopmental disorders and yet its origins remain unknown. Polymer gel models suggest that wrinkling emerges spontaneously due to compression forces arising during differential swelling, but these ideas have not been tested in a living system. Here, we report the appearance of surface wrinkles during the in vitro development and self-organization of human brain organoids in a microfabricated compartment that supports in situ imaging over a timescale of weeks. We observe the emergence of convolutions at a critical cell density and maximal nuclear strain, which are indicative of a mechanical instability. We identify two opposing forces contributing to differential growth: cytoskeletal contraction at the organoid core and cell-cycle-dependent nuclear expansion at the organoid perimeter. The wrinkling wavelength exhibits linear scaling with tissue thickness, consistent with balanced bending and stretching energies. Lissencephalic (smooth brain) organoids display reduced convolutions, modified scaling and a reduced elastic modulus. Although the mechanism here does not include the neuronal migration seen in vivo, it models the physics of the folding brain remarkably well. Our on-chip approach offers a means for studying the emergent properties of organoid development, with implications for the embryonic human brain.

Wrinkling and folding appear universally during the growth of soft and natural systems[1–5]. During brain development, wrinkling occurs at two stages: first, the emergence of folds along the neural tube separates and defines different brain regions, such as the left and right hemispheres[6,7]. Second, folding of the cortex contributes to the expansion of brain surface area[8–10]. Reduced cortical folding (lissencephaly) is one of the manifestations of a severe neurodevelopmental disorder, which is accompanied with intellectual disability and reduced life expectancy[11,12]. From a physical perspective, surface wrinkles emerge as a mechanical instability when an elastic material is under compression[13]. At low forces, the material is compressed in the direction of the force and expands perpendicular to it, thus resulting in strain. Beyond a critical force, the material will exhibit folding and wrinkling to release the compression, without further increase in strain energy. Compression forces and wrinkling can arise internally during differential swelling of polymer gels, due to solvent absorption[14–19]. When the outer region of a gel is swelling faster than the interior, the mismatch leads to residual strain and results in periodic wrinkling. Similarly, wrinkling can arise during in vivo development both from non-homogeneous tissue growth[20], and localized cytoskeletal contraction[5,21,22]. Here, we study the emergence of folding during in vitro brain organoid development, characterize the physical mechanisms which lead to differential growth, and reveal the underlying critical and scaling behaviour.

Recent breakthroughs in stem-cell technologies enable three-dimensional culturing of human stem cells, which develop into organ-like structures, and exhibit remarkable self-organization and collective behaviour ('organoids')[23–28]. However, three-dimensional growth to a millimetre scale without vasculature leads to cell death in the organoid core, as diffusion becomes inefficient for nutrient supply. Furthermore, tissue thickness obstructs optical imaging and real-time microscopy is carried out in organoid slices. Here, we present an on-chip approach, which enables development of human brain organoids to millimetre diameter, together with efficient nutrient exchange by diffusion, and in situ whole-organ fluorescent live imaging over several weeks.

Human embryonic stem cell aggregates were inserted into a microfabricated compartment[29] of height $h=150\pm10\,\mu$m, and filled with collagen-laminin-based hydrogel (Matrigel™) (Fig. 1a-d, Supplementary Fig. S1, Methods). Within 1–3 days, the homogeneous and isotropic cell aggregate self-organized into a spherical shell structure surrounding a small cavity (lumen) (Fig. 1e, Day 3, Supplementary Fig. S2). During the first week, the organoid expanded by a factor of 20 to an area of $0.2\pm0.05\text{mm}^2$ and a thickness of $t=50$–$200\,\mu$m (Fig. 1e Day 4–6, Supplementary Figs. S3, S4). The cells in the organoid attained a bipolar morphology, extending from the inner (apical) surface of the organoid, $r=0$, to the outer (basal) surface, $r=t$ (Fig. 1d). The cell nuclei were radially oriented (Fig. 1d) and performed an up-and-down radial motion coupled to the cell cycle, with cell division at the inner surface, $r=0$ (Supplementary Movie S1). This mimics the developing brain ventricular zone, which is composed of proliferating neuronal stem cells[30]. The developing organoid exhibited enrichment of cerebral cortex specific genes[31], including FOXG1, PAX6, EMX2 and LHX2, as revealed by RNA sequencing (Fig. 1f, Supplementary Fig. S5), and an increase in genes typical for radial glia cells and neurons, accompanied by a corresponding decrease in pluripotent cell markers (Supplementary Figs. S5,6). By day 30, immunostaining revealed a layer of NEUN$^+$ neurons surrounding the PAX6$^+$ progenitor cells (Supplementary Fig. S7). These findings indicate that the on-chip organoid approach successfully mimics the early developing cortex.

In the second week of development we observed the emergence of surface instabilities (Fig. 1e; days 6–11). The two-dimensional wrinkling index, $W=\frac{L_G}{L_f}$ was computed as the contour length, L_G, normalized by the length, L_f, of an outer convex contour averaged over $N=14$ organoids (Fig. 2a,c). The wrinkling dynamics exhibited an onset at days 6–8, followed by a maximal wrinkling

[1]Department of Molecular Genetics, Weizmann Institute of Science, Rehovot, Israel. [2]Department of Chemical Research Support, Weizmann Institute of Science, Rehovot, Israel. *e-mail: orly.reiner@weizmann.ac.il

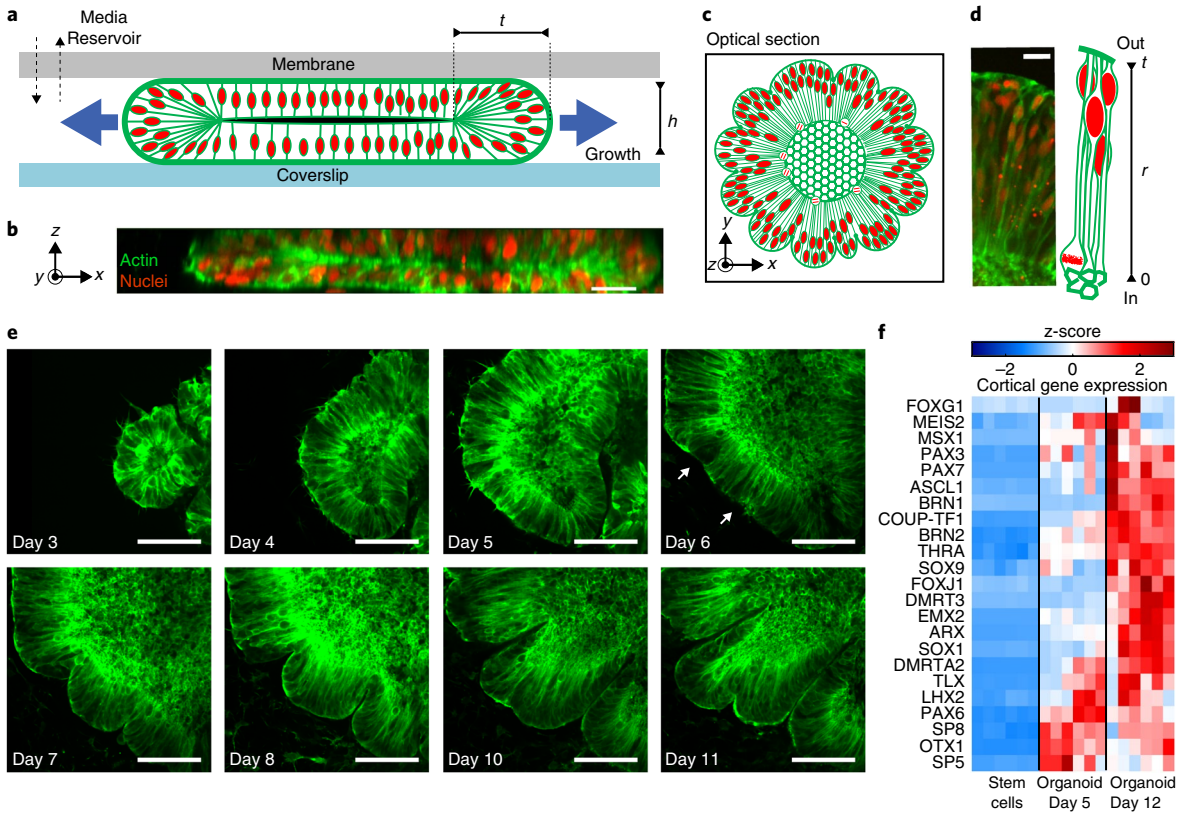

Fig. 1 | Brain organoid development and wrinkling. a, Illustration of the two-dimensional compartment, $h = 150\,\mu m$. The organoid thickness is t. The top membrane is coupled to a media reservoir, and the bottom coverslip enables in situ imaging. **b**, Z-stack image of the organoid showing actin using Lifeact-GFP (green) and cell nuclei using H2B-mCherry (red). **c**, Illustration of an organoid optical section. **d**, Fluorescence image and illustration showing cell organization in the organoid. Dashed white line marks inner organoid surface surrounding a lumen. Cells exhibit a bipolar morphology, stretched between the outer surface ($r = t$) and the inner surface ($r = 0$). Nuclei are distributed along the radial coordinate, and cell division occurs at the inner surface ($r = 0$). **e**, Fluorescence images showing the development of the organoid during days 3–11 after Matrigel embedment, and the emergence of wrinkles. Arrows indicate initial wrinkling instability. **f**, RNA sequencing expression data in the organoids for three developmental time points: embryonic stem cell culture, and organoids 5 and 12 days after Matrigel embedment. Six samples are shown for each time point (three wild-type and three *LIS1* +/− mutants). Colour bar indicates the row z-score. The list contains genes that are typical for telencephalon and cortical brain regions. Scale bars are 100 μm (**e**), 50 μm (**b**), 20 μm (**d**).

rate at days 10–12, and saturation at a maximal average value $< W_{max} > = 2.1 \pm 0.1$ at day 15. Similar folds appeared in devices with a reduced hydrogel density, and with anti-adhesive materials: PEG hydrogel and Lipidure (Supplementary Figs. S8,9).

We next studied the cellular structure of the organoid, and observed that the number of nuclei per unit area ρ (nuclear density, Fig. 2b,d), as well as the nuclear aspect ratio R_1/R_2 (Fig. 2e), increased during days 1–6, before the onset of wrinkling. Nuclear data was averaged from five organoids, in each of which more than 50 nuclei were measured. Nuclear density was measured at the outer region, $r/t > 0.5$, and normalized by the average nuclear area $<a> = 89 \pm 14\,\mu m^2$ (Supplementary Fig. S10). At the wrinkling onset, the nuclear aspect ratio reached a maximal value $<R_1/R_2> = 2.6 \pm 0.1$ (Day 8), followed by a decrease to a value of $<R_1/R_2> = 2.2 \pm 0.1$ (Day 16). The nuclear density saturated exponentially at a maximal value, at $<\rho_{max}> = 1.00 \pm 0.05 <a>^{-1}$, suggesting that the nuclei physically encompass all the available area.

Plotting the wrinkling index as a function of nuclear density, we observed a sharp transition to wrinkling at a critical density $\rho_c = 0.85 \pm 0.1 <a>^{-1}$ (Fig. 2f). These data suggest that during organoid growth the nuclei undergo compression, as manifested by the increase in aspect ratio and density. As the compression reaches a critical value, the organoid surface wrinkles (Fig. 2g). We next exploited the range of organoid thickness, $50 < t < 200\,\mu m$, to study the wrinkle wavelength λ as a function of thickness t (Fig. 2h). Strikingly, in the region $t < 125\,\mu m$ we observed a linear scaling $\lambda \propto 0.8t$. Beyond $t > 125\,\mu m$, the wavelength saturates at a maximal value, $\lambda = 125 \pm 8\,\mu m$. A similar scaling behaviour, $\lambda \propto t \left(\frac{E_s}{E_B}\right)^{1/3}$, was previously observed in polymer gel systems and theoretical models, in which a swelling outer layer of thickness t and elastic modulus E_s is constrained by a non-swelling bulk with elastic modulus E_B[13,17,18] (Fig. S11). In the following paragraphs, we provide evidence that the organoid undergoes differential swelling due to cell-cycle-dependent nuclear swelling and motion, and due to cytoskeleton contraction at the organoid inner surface.

Nuclear position and area were analysed in the growing organoid over 48 h (Fig. 3, Supplementary Movie S1). The nuclei performed a periodic in–out motion, which was coupled to the cell cycle (Fig. 3a,b, Supplementary Fig. S12). This phenomenon is known as interkinetic nuclear movement and is one of the hallmarks of the brain ventricular zone in vivo[30,32–34]. The nuclear motion included a stationary phase close to the outer surface, rapid motion towards the inner surface, division into two daughter cells, followed by an outward motion. Nuclear velocities during motion reach $v = 10$–$30\,\mu m\,h^{-1}$, consistent with in vitro two-dimensional human cell culture measurements[35] (Fig. 3c). The outward velocities decay as the nuclei move away from the inner (apical) surface, $v_{out} \propto 1/r$. The inward velocities follow the same trend with an additional high-velocity

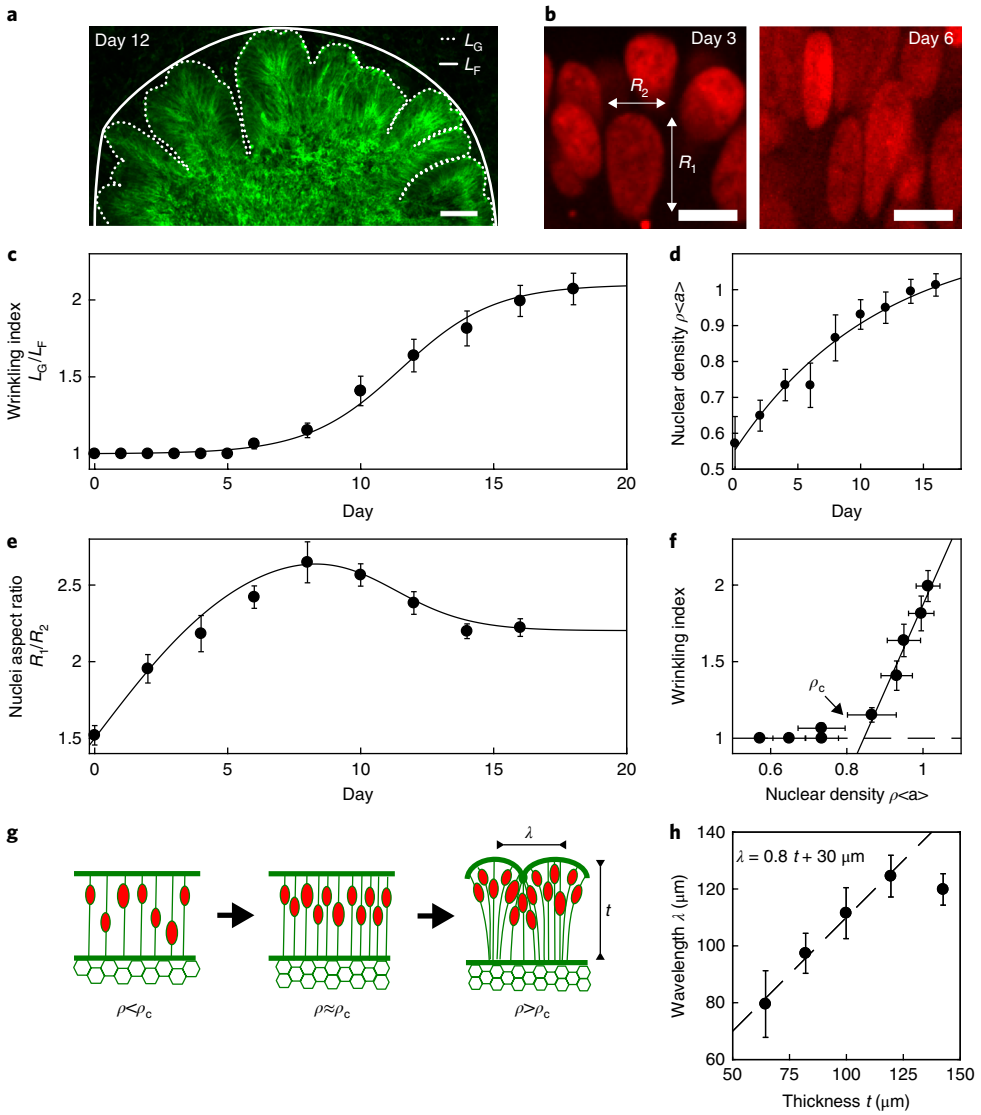

Fig. 2 | Organoid wrinkling occurs at a critical nuclear density and maximal strain. a, A low-magnification image of the wrinkled organoid. Dotted line marks the organoid contour of length L_G. Solid line marks a convex contour of length L_F. **b**, Fluorescence images of H2B-mCherry showing nuclear aspect ratio and density for days 3,6. **c**, Wrinkling index $W = L_G/L_F$ as a function of time averaged over 14 organoids. **d**,**e**, Nuclear density ρ and aspect ratio R_1/R_2, respectively, as a function of time averaged over 250 nuclei sampled from five organoids, with 50 nuclei each. **f**, Wrinkling index as a function of nuclear density ρ (nuclei per area). Nuclear density was measured at the tissue outer region, $r/t>0.5$, and normalized by the average nuclear area $<a> = 89 \pm 14\,\mu m^2$. A sharp wrinkling transition is observed at a critical density $\rho_c = 0.85 \pm 0.1 <a>$. **g**, Illustration showing organoid wrinkling at a critical density ρ_c. **h**, Wrinkling wavelength λ as a function of thickness t, exhibiting a linear scaling regime. Scale bars are 100 μm (**a**), 10 μm (**b**). Error bars represent s.e.m.

phase in the range $0.4<r/t<0.8$. At steady-state, we expect that nuclear density is inversely proportional to the nuclear velocities, such that nuclei accumulate at positions where their motion is slow. Indeed, the nuclear density profile exhibits a linear dependence, $\rho \propto r$, which is inversely proportional to the slow outward velocity, $\rho \propto 1/v_{out}$ (Fig. 3d). Overall, the active motility of the nuclei is a mechanism by which material is actively transported to the outer organoid regions, slows down, and accumulates. This implies that the outer regions of the organoid grow faster than the inner regions. Notably, the density profile becomes nonlinear following the wrinkling onset (Supplementary Fig. S13b).

We further studied nuclear growth during the cell cycle, by measuring the nuclear area, A, as a function of the nuclear radial position, r/t (Fig. 3e). Nuclei undergo a twofold area increase as they move inwards from the outer surface ($r_1/t \approx 0.9$, $A_1 \approx 75\,\mu m^2$) towards the inner region ($r_2/t \approx 0.25$, $A_2 \approx 150\,\mu m^2$). Cells undergo mitosis at the inner surface, preceded by rapid DNA condensation ($r_3/t<0.1$, $A_2 \approx 50\,\mu m^2$). The two newly-born nuclei perform an outward motion with a small change in area. The increase in nuclear area during the cell cycle period is 40% higher in the outer part of the organoid, $r/t>0.5$, than the inner part of the organoid, $r/t<0.5$ (Fig. 3f). This is consistent with the cell-cycle synthesis (S) phase, which occurs near the basal (outer) surface of the ventricular zone in vivo[30]. Thus, the cell-cycle-dependent nuclear position and biosynthesis leads to increased swelling in the outer region of the organoid (Fig. 3g).

We next studied the role of cell contractility in the organoid. We administered a low concentration (5 μM) of blebbistatin, which inhibits myosin contractility, during days 6–10 (Fig. 4a). The drug-treated organoids had a smoother basal (outer) surface, in comparison to control organoids (Fig. 4b). In addition, the treated organoids exhibited a higher apical (inner) surface curvature than the control

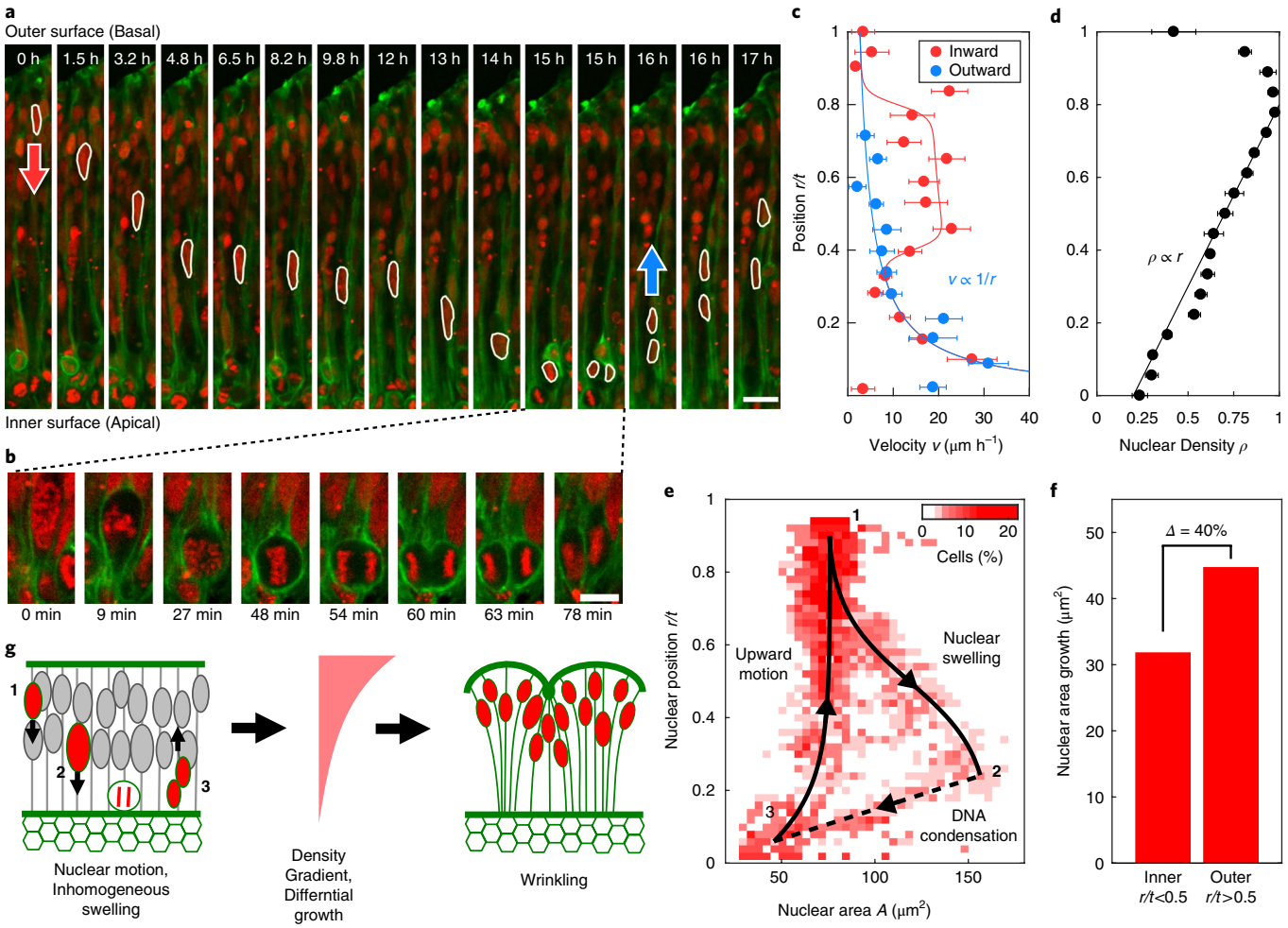

Fig. 3 | Nuclear motion and swelling during cell cycle lead to differential growth. a, Time-lapse fluorescence images of nuclear motion in the organoid during the cell cycle. H2B-mCherry (red) and Lifeact-GFP (green). **b**, High-resolution images during cell mitosis at the inner surface. **c**,**d**, Nuclear velocities v and nuclear density ρ, respectively, as a function of radial position r/t. Velocities were measured for both inward (red) and outward (blue) motions. **e**, Two-dimensional phase-space diagram of nuclear area A and radial-position r/t. Red colour intensity indicates the percentage of nuclei at each point. The nuclei distribution is limited to a closed path, reflecting the periodic cell cycle. (1→2) Nuclear swelling: two-fold increase in nuclear area, coupled with an inward nuclei motion. (2→3) DNA condensation: motion towards the mitosis region at the inner surface, and decrease in area during DNA condensation prior to cell division. (3→1) Upward motion of 'newly born' nuclei. Data was taken from analysis of 13 nuclei over 48 h with a time step of 3 min. Black line and arrows were drawn to indicate progression with time. **f**, Nuclear area growth, during a cell cycle period, in the outer half of the organoid (r/t>0.5) compared to the inner half of the organoid (r/t<0.5). **g**, Illustration of a physical mechanism for wrinkling. Nuclear motion and position-dependent nuclear swelling create density and growth gradients, which are maximal at the organoid outer regions. The differential growth leads to residual stress and wrinkling. Scale bars are 20 μm (**a**) and 10 μm (**b**). Error bars represent s.e.m.

organoids. The curvature was measured by averaging the tangent angle $\theta(r)$ derivative along the surface perimeter contour $<\partial_r\theta(r)>$ in 7–10 organoids. Notably, the effect of blebbistatin was irreversible. By comparing our results against the swelling gel model[17], we conclude that the cytoskeleton inhibition drug effectively acts to soften the elasticity of the organoid core, E_B. A soft core, $E_B<E_S$, is easily pulled and follows the outer surface folds, allowing long-wavelength (small-curvature) folds. In contrast, a stiff core, $E_B \gg E_S$, retains its original shape during the swelling process and results in short-wavelength folds and high curvature.

Next, we studied the short-term effects of cytoskeleton inhibition, using blebbistatin (Fig. 4c), nocodazole, which disturbs microtubules polymerization, and Rho-associated coiled-coil containing protein kinase (ROCK) inhibitor, which disrupts myosin contractility and actin polymerization[22]. Additionally, we used laser microdissection to irradiate cells in the organoid core, while keeping the perimeter cells intact (Fig. 4d, Supplementary Fig. S14). All treatments resulted in expansion of the inner surface (Fig. 4c,d), and a reduction in perimeter thickness (Fig. 4e). Blebbistatin treatment resulted in an increase of the cellular inner surface area from $19\pm0.5\,\mu m^2$ to $50\pm2\,\mu m^2$ (Fig. 4f). Laser microdissection resulted in a relative inner surface area of $12\pm2\%$ (Supplementary Fig. S14). The neuroepithelium thickness after the treatment, t, is described by a single linear function of the thickness before treatment, t_0, for all drugs and including the microdissection (Fig. 4e,i). The reduction in thickness is $\Delta t = t - t_0 = -0.22t_0 - 5\,\mu m$ (Fig. 4e). Lifeact-GFP fluorescence intensity along the inner surface was reduced (Fig. 4h,j), which is attributed to disassembly of actomyosin filaments. The outer surface fluorescence increased, which may be due to redistribution of actin within the cell, as the total amount of actin is preserved. Additionally, a decrease in the aspect ratio of the nucleus was observed from $R_1/R_2 = 2.6\pm0.3$ before treatment, to $R_1/R_2 = 1.9\pm0.1$ after blebbistatin treatment, and $R_1/R_2 = 2.02\pm0.16$ after treatment with ROCK inhibitor (Fig. 4k,l). Overall, these data

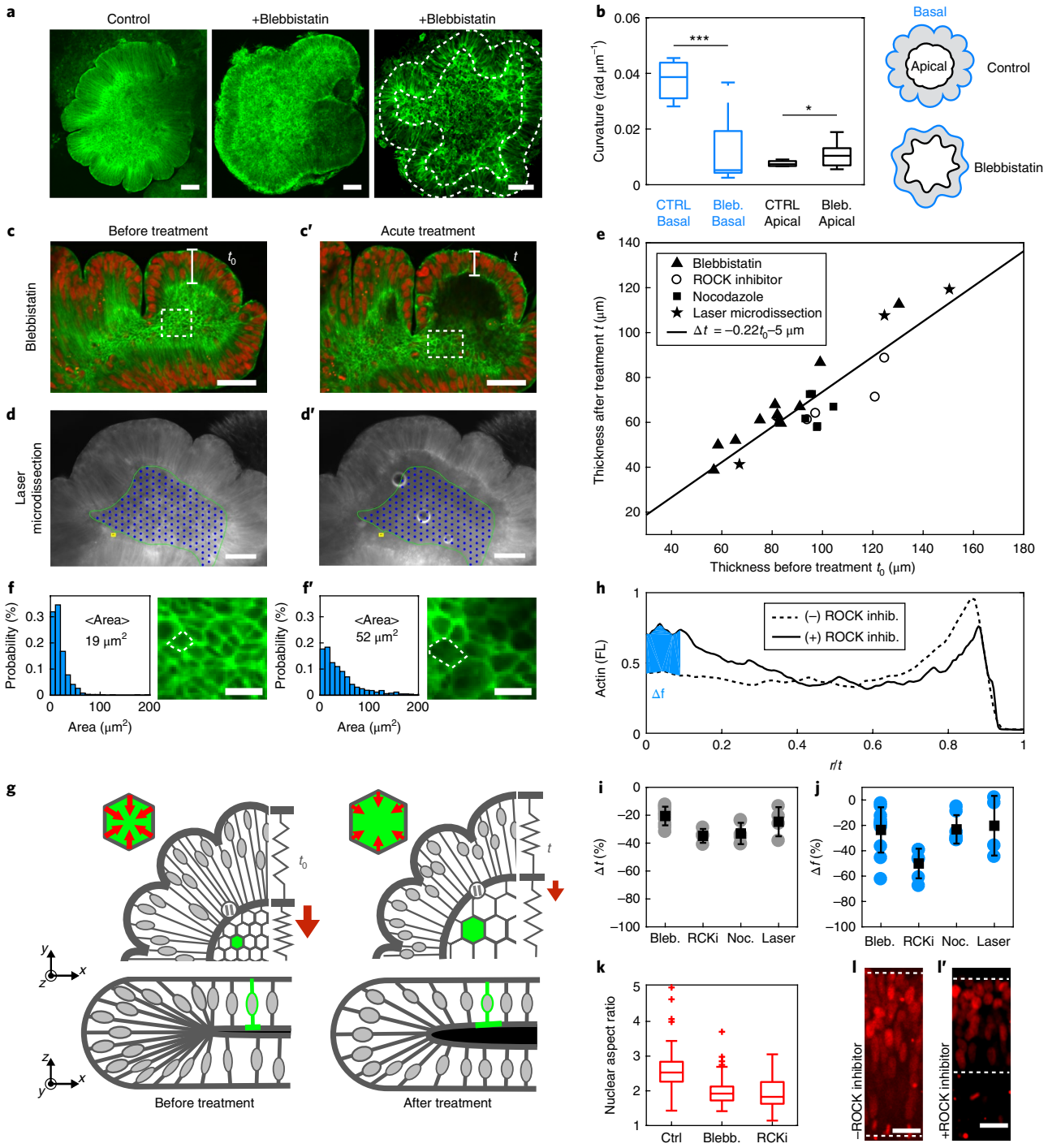

Fig. 4 | Cytoskeletal forces maintain organoid core contraction and stiffness. a, Images of organoids treated with blebbistatin (+Blebbistatin) during days 6–10 and control. Dashed lines mark inner and outer surfaces. **b**, Average curvature $<|\partial_s\theta(r)|>$ of outer (basal, blue) and inner (apical, black) organoid surfaces for control (CTRL) and treated (Bleb.) organoids ($N = 7$–10). **c**,**d**, Images of organoids before and after acute treatment with cytoskeleton disturbing drugs including blebbistatin (**c**,**c′**) and laser microdissection treatment of the organoid core (marked with green line and blue dots) (**d**,**d′**). **e**, Organoid thickness before (t_0) and after (t) cytoskeleton disturbing treatments including blebbistatin, ROCK inhibitor, nocodazole and laser microdissection. **f**,**f′**, Magnified view of (**c**,**c′**) reveals that the inner surface area of cells is increased following drug treatment. **g**, Illustration of the organoid during cytoskeleton inhibition, showing the reduction in thickness and increase in inner surface area. **h**, Lifeact fluorescence profile along the radial coordinate r/t before (solid line) and after (dashed line) treatment with ROCK inhibitor. Blue area marks the difference in fluorescence intensity at the inner surface ($0<r/t<0.1$). **i**,**j**, Reduction in inner surface thickness (**i**) and fluorescence (**j**) surface fluorescence (**i**) and thickness (**j**) for drug and microdissection treatments. Averages (squares) taken over 4–11 repeats (circles) for each condition. **k**, Nuclear aspect ratio in control organoids (Ctrl) and after treatments. Data include 40–70 nuclei from three organoids. **l**,**l′**, H2B-mCherry fluorescence images before and after treatment. Dashed lines indicate inner and outer surfaces. Scale bars are 100 µm (**a**,**d**), 50 µm (**c**), 20 µm (**l**) and 10 µm (**f**). Error bars represent s.e.m. Asterisks represent statistical significance ($*p<0.05$, $***p<0.001$) (**b**). The horizontal line within the box plots (**b**,**k**) indicates the median, boundaries of the box indicate the 25th and 75th percentile, whiskers cover 99.3 percent of data, and red crosses indicate outliers.

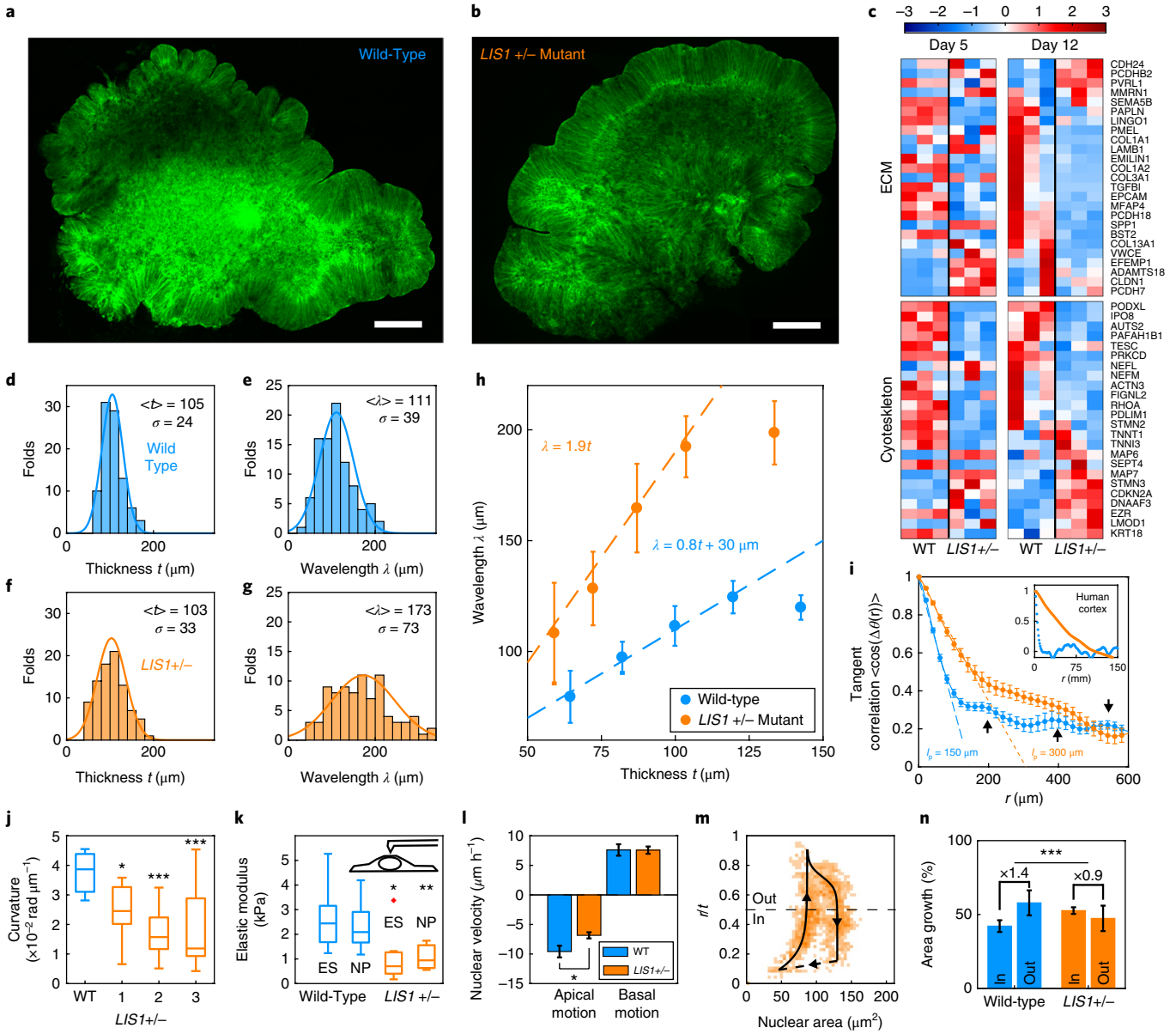

Fig. 5 | *LIS1*+/− mutation results in lissencephalic organoids, modified ECM and cytoskeleton, and reduced cell elasticity. a,**b**, Images of wild-type (WT) and *LIS1* mutant organoids (*LIS1*+/-), respectively. **c**, Expression data of extra cellular matrix (ECM) and cytoskeleton related genes ($N=3$). **d**–**g**, Distribution of organoid thickness (**d**,**f**) and wrinkling wavelength (**e**,**g**) for WT (**d**,**e**) and *LIS1*+/− (**f**,**g**) ($N=5$). **h**, Wrinkle wavelength as a function of thickness. **i**, Tangent correlation function, $<\cos(\theta(\Delta r))>$, between two points at a distance r along the organoid surface ($N=9$ WT, 10 *LIS1*+/−). At short distances the correlation decreases linearly, $1-r/l_p$. WT organoids exhibit correlation peaks (arrowheads). Inset: correlation functions of healthy (blue) and lissencephalic (orange) human brains. **j**, Average curvature $<|\partial_t\theta(r)|>$ of WT and three different and isogenic *LIS1*+/− clones ($N=9$–11). **k**, Elastic modulus of WT and *LIS1*+/− embryonic stem cells (ES) and neuronal progenitors (NP) from several thousand force curves ($N=7$–10). Inset, an illustration of AFM measurements. **l**, Nuclear velocities during apical (inward) and basal (outward) motion for WT and *LIS1*+/− ($N=15$). **m**, Two-dimensional diagram of nuclear area A and radial-position r/t of *LIS1*+/− nuclei. Orange colour intensity indicates the percentage of nuclei at each point. Black line and arrows indicate progression with time. **n**, Nuclear area growth, over a cell-cycle period, in the outer (Out, $r/t>0.5$) and inner (In, $r/t<0.5$) parts of the organoid for WT (same as Fig. 2f) and *LIS1* +/−. Kolmogorov–Smirnov test was used to compare the WT and *LIS1*+/− distributions. Scale bars are 200 μm (**a**,**b**), 50 μm (**c**) and 5 μm(**n**). Error bars represent s.e.m. Asterisks represent statistical significance ($^*p<0.05$,$^{**}p<0.01$,$^{***}p<0.001$). The horizontal line within the box plots (j,k) indicates the median, boundaries of the box indicate the 25th- and 75th -percentile, whiskers cover 99.3 percent of data, and red crosses indicate outliers.

indicate that the apical surface is actively contracted by the cellular cytoskeleton, and contributes to the effective stiffness of the organoid core (Fig. 4g).

We next studied the effect of *LIS1* heterozygous (+/−) mutation (Fig. 5a,b). The mutation is associated with lissencephaly, which is a severe smooth brain malformation[11,36,37]. The LIS1 protein is involved in several key functions, including proliferation and neuronal migration, as well as in the regulation of molecular motors and the cell cytoskeleton[38–45]. Three isogenic mutant cell-line clones were generated, using CRISPR/Cas9 genome editing, and expressed reduced LIS1 protein levels (Supplementary Fig. S15). The *LIS1*+/− organoids followed the same neuronal development pathway as

the wild-type organoids, as observed by elevation of telencephalon-related genes (Supplementary Figs. S5,6, Pearson coefficient 0.98). Cytoskeleton and extra cellular matrix (ECM) related genes exhibited significant differential expression between wild-type and *LIS1*+/− organoids (Fig. 5c, Supplementary Fig. S5). ECM has been suggested to play an important role in the evolutionary expansion of the neocortex and its gyrification, especially within a unique subpopulation of basal or outer radial glia progenitors[46,47].

We compared the folding of wild-type and mutant organoids (days 6–8, Fig. 5d–g, $N=5$ organoids). For the wild-type organoids, the mean wrinkle wavelength was similar to the mean thickness during wrinkling onset, $\langle\lambda\rangle\approx\langle t\rangle\approx 100\,\mu$m (Fig. 5d,e). We observed Gaussian distributions for the organoid thickness, $\sigma_t=24\,\mu$m, and for the wavelength, $\sigma_\lambda=39\,\mu$m. In the *LIS1* +/− mutant we observed broadening of the Gaussian distribution for t, with no significant change in mean value (Fig. 5f). In contrast, the average wavelength $\langle\lambda\rangle\approx 170\,\mu$m was significantly longer ($p<0.001$), and the distribution was wider $\sigma_\lambda=70\,\mu$m (Fig. 5g). Notably, the *LIS1* +/− organoids exhibited linear scaling of wavelength with thickness, similar to the wild-type organoids, but with an increased prefactor, $\lambda_{LIS1}\propto 1.9t$ (Fig. 5h). Beyond $t>100\,\mu$m, the wavelength saturated at a maximal value, $\lambda_{LIS1}=200\pm15\,\mu$m.

The wrinkling morphology was further analysed by measuring the surface tangent angle $\theta(r)$ of developed organoids (days 16–18, Fig. 5i,j). We computed the organoid curvature by averaging the tangent derivative along the organoid perimeter $\langle\partial_r\theta(r)\rangle$ (Fig. 5j, Supplementary Figs. S16–18, $N=9$–11). We observed a significant reduction in the *LIS1* +/− organoid curvature, for all three clones, in comparison to the wild-type. We further computed the tangent correlation function, $\langle\hat{t}(r)\,\hat{t}(r+\Delta r)\rangle=\langle\cos(\Delta\theta(r))\rangle$ (Fig. 5i). The correlation exhibited a sharp linear decrease at short distances, $\langle\cos(\Delta\theta(r))\rangle\approx 1-r/l_p$, with persistence length $l_p=148\pm11\,\mu$m (wild-type), and $l_p=306\pm11\,\mu$m (mutant). At long distances we observed three correlation peaks for the wild-type organoids, $r=200\,\mu$m, 380 μm, 520 μm. The peaks indicated a periodic structure $\lambda_\theta=180\pm15\,\mu\text{m}\approx\langle W\rangle\,\langle\lambda\rangle$ consistent with the measured wavelength, $\langle\lambda\rangle\approx 110$, and the maximal wrinkling index of $\langle W\rangle=2.1$. In contrast, the mutant organoid did not exhibit correlation peaks. The main features of the wild-type correlation function persisted in an analysis of a healthy human brain, which exhibited multiple wavelength peaks (Fig. 5i, inset). Analysis of a lissencephalic brain resulted in a longer persistence length, and a lack of correlation peaks. The aberrant *LIS1* +/− expression of ECM and cytoskeleton related genes, together with the modified wavelength scaling prefactor, suggested that the *LIS1* +/− cells have different elastic properties than wild-type cells. To test this, individual cells were analysed using atomic force microscopy (AFM) as embryonic stem cells (ES), and as neuronal progenitors (NP). The wild-type cells exhibited elastic modulus $E^{\mathrm{NP}}_{\mathrm{WT}}=2.7\pm0.5$ kPa and $E^{\mathrm{ES}}_{\mathrm{WT}}=2.4\pm0.4$ kPa, similar to previous measurements[48] (Fig. 5k, Supplementary Figs. S19,20). Remarkably, the *LIS1* +/− mutant cells were significantly softer than the wild-type cells by a approximately a factor of 2., $E^{\mathrm{NP}}_{LISis1}=1\pm0.2$ kPa ($p<0.005$) and $E^{\mathrm{ES}}_{LISis1}=1.1\pm0.4$ kPa ($p<0.05$). Thus, our findings indicate that the *LIS1* +/− modified wrinkling stems from 'softening' of the cytoskeleton, similar to the blebbistatin treatment (Fig. 4b), and is analogous to reduction of the bulk elastic modulus, E_B, in the polymer gel model[17].

Furthermore, *LIS1* +/− organoids exhibited significantly reduced velocities during inward motion of the nuclei, $v_{LIS}=-6.8\pm0.5$, compared to wild-type, $v_{\mathrm{WT}}=-9.6\pm1$, $p<0.05$ (Fig. 5l, Supplementary Movie S2). Additionally, the *LIS1* +/− nuclear swelling profile was different from that of the wild-type, $p<10^{-3}$ (Fig. 5m,n). The reduction in differential growth may contribute to the reduction in *LIS1*+/− wrinkling. Finally, the response of *LIS1* +/− organoids to the drug treatments was similar to that observed in the wild-type organoids (Supplementary Fig. S21).

Taken together, our data suggest that the organoid wrinkling is driven by a mechanical instability, which is universal for differentially swelling materials. The increased growth in the organoid outer regions, together with the actively contracting organoid inner surface, both contribute to the emergent wrinkling pattern. The presented three-dimensional organization of the organoid, gene expression data and nuclei motion indicate that the on-chip organoid approach successfully mimics the early developing cortex.

We next compared the organoid wrinkling to cortical gyrification. The periodic folding morphology and temporal dynamics are remarkably similar to MRI images of fetal brains[18,20,49]. The nuclear motion leads to differential growth mechanism, analogous to the way radial neuronal migration may play a role in brain folding[50]. However, cortical gyrification occurs around week 30 of embryonic development, when the cell population is largely composed of neurons. This is in contrast to the organoids, which are composed of neuronal progenitors, and model an earlier developmental time point. Thus, while organoid wrinkling results from differential growth of progenitor cells, and includes cell-cycle-dependent changes in nuclear size, cortical folding is hypothesized to be driven by crowding of non-dividing neurons which are migrating towards the surface of the brain. In addition, apical contraction seems to play a significant role in organoid wrinkling, which has not been observed in cortical folding, and may be opposed by the hydrostatic pressure of the cerebral fluid in vivo. Finally, a *LIS1* +/− mutation led to reduction in organoid wrinkling, involving changes in nuclear motion, ECM and cytoskeleton. However, smooth brains of *LIS1* +/− patients are widely accepted to reflect a defect in neuronal migration, a process not modelled here. Thus, while the organoid wrinkling is remarkably analogous to cortical gyrification, there are significant biological and physical differences. Overall, the on-chip organoids provide a novel model system to study the physics and biology of early human brain development, and reveal the mechanism of wrinkling in a living system.

Received: 22 June 2017; Accepted: 8 January 2018;
Published online: 19 February 2018

References

1. Hannezo, E., Prost, J. & Joanny, J.-F. Mechanical instabilities of biological tubes. *Phys. Rev. Lett.* **109**, 018101 (2012).
2. Shraiman, B. I. Mechanical feedback as a possible regulator of tissue growth. *Proc. Natl. Acad. Sci. USA* **102**, 3318–3323 (2005).
3. Klein, Y., Efrati, E. & Sharon, E. Shaping of elastic sheets by prescription of non-Euclidean metrics. *Science* **315**, 1116–1120 (2007).
4. Savin, T. et al. On the growth and form of the gut. *Nature* **476**, 57–62 (2011).
5. Kim, H. Y., Varner, V. D. & Nelson, C. M. Apical constriction initiates new bud formation during monopodial branching of the embryonic chicken lung. *Development* **140**, 3146–3155 (2013).
6. Kiecker, C. & Lumsden, A. Compartments and their boundaries in vertebrate brain development. *Nat. Rev. Neurosci.* **6**, 553–564 (2005).
7. Taber, L. A. Morphomechanics: transforming tubes into organs. *Curr. Opin. Genetics Dev.* **27**, 7–13 (2014).
8. Sun, T. & Hevner, R. F. Growth and folding of the mammalian cerebral cortex: from molecules to malformations. *Nat. Rev. Neurosci.* **15**, 217–232 (2014).
9. Florio, M. & Huttner, W. B. Neural progenitors, neurogenesis and the evolution of the neocortex. *Development* **141**, 2182–2194 (2014).
10. Mota, B. & Herculano-Houzel, S. Cortical folding scales universally with surface area and thickness, not number of neurons. *Science* **349**, 74–77 (2015).
11. Reiner, O. et al. Isolation of a Miller–Dieker lissencephaly gene containing G protein beta-subunit-like repeats. *Nature* **364**, 717–721 (1993).
12. Reiner, O. & Sapir, T. LIS1 functions in normal development and disease. *Curr. Opin. Neurobiol.* **23**, 951–956 (2013).
13. Groenewold, J. Wrinkling of plates coupled with soft elastic media. *Phys. A* **298**, 32–45 (2001).
14. Tanaka, T. et al. Mechanical instability of gels at the phase transition. *Nature* **325**, 796–798 (1987).
15. Bowden, N. et al. Spontaneous formation of ordered structures in thin films of metals supported on an elastomeric polymer. *Nature* **393**, 146–149 (1998).

16. Cerda, E. & Mahadevan, L. Geometry and physics of wrinkling. *Phys. Rev. Lett.* **90**, 074302 (2003).
17. Dervaux, J., Couder, Y., Guedeau-Boudeville, M. A. & Ben Amar, M. Shape transition in artificial tumors: From smooth buckles to singular creases. *Phys. Rev. Lett.* **107**, 018103 (2011).
18. Tallinen, T., Chung, J. Y., Biggins, J. S. & Mahadevan, L. Gyrification from constrained cortical expansion. *Proc. Natl Acad. Sci. USA* **111**, 12667–12672 (2014).
19. Tallinen, T. et al. On the growth and form of cortical convolutions. *Nat. Phys.* **12**, 588–593 (2016).
20. Budday, S., Raybaud, C. & Kuhl, E. A mechanical model predicts morphological abnormalities in the developing human brain. *Sci. Rep.* **4**, 5644 (2014).
21. Gutzman, J. H., Graeden, E. G., Lowery, L. A., Holley, H. S. & Sive, H. Formation of the zebrafish midbrain–hindbrain boundary constriction requires laminin-dependent basal constriction. *Mech. Dev.* **125**, 974–983 (2008).
22. Lecuit, T. & Lenne, P.-F. Cell surface mechanics and the control of cell shape, tissue patterns and morphogenesis. *Nat. Rev. Mol. Cell Biol.* **8**, 633–644 (2007).
23. Eiraku, M. et al. Self-organized formation of polarized cortical tissues from ESCs and its active manipulation by extrinsic signals. *Cell Stem Cell* **3**, 519–532 (2008).
24. Lancaster, M. A. et al. Cerebral organoids model human brain development and microcephaly. *Nature* **501**, 373–379 (2013).
25. Paşca, A. M. et al. Functional cortical neurons and astrocytes from human pluripotent stem cells in 3D culture. *Nat. Methods* **12**, 671–678 (2015).
26. Clevers, H. Modeling development and disease with organoids. *Cell* **165**, 1586–1597 (2016).
27. Bershteyn, M. et al. Human iPSC-derived cerebral organoids model cellular features of lissencephaly and reveal prolonged mitosis of outer radial glia. *Cell Stem Cell* **20**, 435–449.e4 (2017).
28. Di Lullo, E. & Kriegstein, A. R. The use of brain organoids to investigate neural development and disease. *Nat. Rev. Neurosci.* **18**, 573–584 (2017).
29. Morel, M., Galas, J.-C., Dahan, M. & Studer, V. Concentration landscape generators for shear free dynamic chemical stimulation. *Lab. Chip.* **12**, 1340–1346 (2012).
30. Miyata, T., Okamoto, M., Shinoda, T. & Kawaguchi, A. Interkinetic nuclear migration generates and opposes ventricular-zone crowding: insight into tissue mechanics. *Front. Cell. Neurosci.* **8**, 473 (2014).
31. Hébert, J. M. & Fishell, G. The genetics of early telencephalon patterning: some assembly required. *Nat. Rev. Neurosci.* **9**, 678–685 (2008).
32. Dantas, T. J., Carabalona, A., Hu, D. J. K. & Vallee, R. B. Emerging roles for motor proteins in progenitor cell behavior and neuronal migration during brain development. *Cytoskeleton* **73**, 566–576 (2016).
33. Tsai, J.-W., Chen, Y., Kriegstein, A. R. & Vallee, R. B. LIS1 RNA interference blocks neural stem cell division, morphogenesis, and motility at multiple stages. *J. Cell Biol.* **170**, 935–945 (2005).
34. Schenk, J., Wilsch-Brauninger, M., Calegari, F. & Huttner, W. B. Myosin II is required for interkinetic nuclear migration of neural progenitors. *Proc. Natl Acad. Sci. USA* **106**, 16487–16492 (2009).
35. Ziv, O. et al. Quantitative live imaging of human embryonic stem cell derived neural rosettes reveals structure–function dynamics coupled to cortical development. *PLoS. Comput. Biol.* **11**, e1004453 (2015).
36. Bi, W. et al. Increased LIS1 expression affects human and mouse brain development. *Nat. Genet.* **41**, 168–177 (2009).
37. Reiner, O. LIS1 and DCX: Implications for brain development and human disease in relation to microtubules. *Sci. (Cairo)* **2013**, 393975 (2013).
38. Sapir, T. Reduction of microtubule catastrophe events by LIS1, platelet-activating factor acetylhydrolase subunit. *EMBO J.* **16**, 6977–6984 (1997).
39. Faulkner, N. E. A role for the lissencephaly gene LIS1 in mitosis and cytoplasmic dynein function. *Nat. Cell Biol.* **2**, 784–791 (2000).
40. Feng, Y. et al. LIS1 regulates CNS lamination by interacting with mNudE, a central component of the centrosome. *Neuron* **28**, 665–679 (2000).
41. Niethammer, M. et al. NUDEL is a novel Cdk5 substrate that associates with LIS1 and cytoplasmic dynein. *Neuron* **28**, 697–711 (2000).
42. Huang, L., Seker, E., Landers, J. P., Begley, M. R. & Utz, M. Molecular interactions in surface-assembled monolayers of short double-stranded DNA. *Langmuir* **26**, 11574–11580 (2010).
43. Egan, M. J., Tan, K. & Reck-Peterson, S. L. Lis1 is an initiation factor for dynein-driven organelle transport. *J. Cell Biol.* **197**, 971–982 (2012).
44. Kardon, J. R. & Vale, R. D. Regulators of the cytoplasmic dynein motor. *Nat. Rev. Mol. Cell Biol.* **10**, 854–865 (2009).
45. McKenney, R. J., Vershinin, M., Kunwar, A., Vallee, R. B. & Gross, S. P. LIS1 and NudE induce a persistent dynein force-producing state. *Cell* **141**, 304–314 (2010).
46. Fietz, S. A. et al. Transcriptomes of germinal zones of human and mouse fetal neocortex suggest a role of extracellular matrix in progenitor self-renewal. *Proc. Natl Acad. Sci. USA* **109**, 11836–11841 (2012).
47. Florio, M. et al. Human-specific gene ARHGAP11B promotes basal progenitor amplification and neocortex expansion. *Science* **347**, 1465–1470 (2015).
48. Guz, N., Dokukin, M., Kalaparthi, V. & Sokolov, I. If cell mechanics can be described by elastic modulus: Study of different models and probes used in indentation experiments. *Biophys. J.* **107**, 564–575 (2014).
49. Gholipour, A. et al. A normative spatiotemporal MRI atlas of the fetal brain for automatic segmentation and analysis of early brain growth. *Sci. Rep.* **7**, 476 (2017).
50. Reillo, I., de Juan Romero, C., García-Cabezas, M. Á. & Borrell, V. A role for intermediate radial glia in the tangential expansion of the mammalian cerebral cortex. *Cereb. Cortex.* **21**, 1674–1694 (2011).

Acknowledgements

We are grateful for the help of S. Viukov, T. Levy and T. Sapir, and for fruitful discussions with S. Safran, A. Tayar and R. Bar-Ziv from the Weizmann Institute of Science. Device fabrication was carried out with assistance from A. Jahanfard, laser microdissection with assistance from Y. Fried, and RNA sequencing and analysis with the advice of H. Keren-Shaul, R. Kohen and T. Olender. Plasmid gifts were received from M. Davidson, Florida State University and J. LoTurco, University of Connecticut. MRI scans were provided by N. Bahi-Buisson, French Institute of Health and Medical Research. O.R. is the incumbent of the Bernstein-Mason Chair of Neurochemistry. E.K. is a Koshland fellow. The research has been supported by the Legacy Heritage Biomedical Program of the Israel Science Foundation (grant no. 2041/16), ERA-NET Neuron with support of the IMOH (grant no. 3-0000-12276), European Cooperation on Science and Technology (COST Action CA16118), Weizmann-FAPESP supported by a research grant from Sergio and Sonia Lozinsky, Nella and Leon Benoziyo Center for Neurological Diseases, Jeanne and Joseph Nissim Foundation for Life Sciences Research, Wohl Biology Endowment Fund, Lulu P. & David J. Levidow Fund for Alzheimers Diseases and Neuroscience Research, the Helen and Martin Kimmel Stem Cell Research Institute, the Kekst Family Institute for Medical Genetics, the David and Fela Shapell Family Center for Genetic Disorders Research. J.H.H. is a New York Stem Cell Foundation (NYSCF)–Robertson Investigator and is supported by research grants from the European Research Council (ERC-CoG2016 CellNaivety), Flight Attendant Medical Research Council (FAMRI), Israel Science Foundation Morasha Program, Nella and Leon Benoziyo Center for Neurological Diseases.

Author contributions

E.K., A.K. and O.R. planned and conducted experiments. S.C. designed and conducted AFM experiments. J.H. planned and assisted in hES-related experiments. The manuscript was prepared with inputs by all the authors.

Competing interests

J.H.H. is an advisor to Biological Industries Ltd and Accelta Ltd, and had issued patent applications and commercial licences related to certain human stem cell methods used herein.

Additional information

Supplementary information is available for this paper at https://doi.org/10.1038/s41567-018-0046-7.

Reprints and permissions information is available at www.nature.com/reprints.

Correspondence and requests for materials should be addressed to O.R.

Publisher's note: Springer Nature remains neutral with regard to jurisdictional claims in published maps and institutional affiliations.

Methods

Device fabrication. The device was fabricated on a commercial 6-cm-diameter polystyrene tissue culture dish (Falcon). Eleven holes of diameter 1.5 mm were drilled at the dish bottom (Supplementary Fig. S1, Step 1). A ultraviolet (UV)-curable adhesive was spread on the bottom surface using a sharp blade (NOA81, Norland Products, Supplementary Fig. S1, step 2). A semi-permeable polycarbonate membrane (Whatman Nuclepore Track-Etched Membranes, pore diameter 0.1 µm) was placed on the adhesive layer (Supplementary Fig. S1, step 3). The device was cured under UV light for 2 min (365 nm 20W LED, Shenzen Yonton Opto). The membrane covered nine drilled holes, thus leaving two holes uncovered, which will serve as inlets. A circular Polydimethylsiloxane (PDMS) stamp of 150 µm thickness and 20 mm diameter was prepared using a metal mold of the same dimensions. The PDMS stamp was placed on a $24\times24\,mm^2$ coverslip (Supplementary Fig. S1, Step 4). The UV-curable adhesive was flowed between the coverslip and PDMS by capillary, thus forming a spacer of thickness 150 µm (Supplementary Fig. S1, Step 5). The spacer was half-cured by UV exposure, and the PDMS was peeled off (Supplementary Fig. S1, Step 6).

Human ESC aggregates. Human embryonic stem cells were cultured on Matrigel-coated plates in Naïve Human Stem-Cell Media (NHSM, Supplementary Table S1) as described elsewhere[51] (Supplementary Fig. S1, Step 7). Cells were dissociated using Trypsin-EDTA (0.05%, ThermoFisher), and diluted in serum-containing media to inhibit trypsin activity. Cells were centrifuged and re-suspended in NHSM with 40 µM Rho Kinase inhibitor Y−27632. The cells were counted and diluted to a final concentration of 2×10^4 cells ml^{-1}. Approximately 600 cells (30 µl) were dispensed into ultra-low cell-attachment 96-plate (Supplementary Fig. S1, Step 8, S-BIO, Hudson, NH, USA). Within several hours cells aggregated at the bottom of the wells (Supplementary Fig. S1, Step 9). After 24 h, 150 µl of Neural Induction Media (Supplementary Table S1) was added.

Device assembly. After 48–72 h, cell aggregates were collected by a pipette and placed on the fabricated culture dish (Supplementary Fig. S1, Step 10). Nine aggregates were placed on top of the membrane-covered holes. The fabricated coverslip was placed on top of the aggregates, thus sealing the device (Supplementary Fig. S1, Step 11). The device was inverted, and the UV-adhesive spacer was fully cured using a mask to protect the cell aggregates. The device was then filled with media and kept in a cell incubator at 37 °C and 5%CO_2 (Supplementary Fig. S1, Step 11). Media was exchanged every other day.

Hydrogel embedment. Five days following the device assembly, collagen-laminin-based hydrogel (100% Matrigel) was injected into the device, and thus embedded the aggregates in a gel environment (Supplementary Fig. S1, Step 13). First, the device was dried. Then, a drop of cool liquid Matrigel was placed on one of the inlets, and a tissue paper was placed on the second inlet. The Matrigel entered the fabricated compartment by capillary force. The device was inserted into the incubator for 25 min for gelification. Finally, Neural Differentiation media (Supplementary Table S1) supplemented with epithelial growth factor (20 ng ml^{-1}, Peprotech AF-100-15) and FGF2 (20 ng ml^{-1}) fibroblast growth factor-basic 2 (20 ng ml^{-1}, Peprotech 100-18B) was added to the device[25] (Supplementary Fig. S1, Step 14). The device was kept in the cell incubator and ready for imaging. Media was exchanged every other day. Several days after Matrigel injection, the homogeneous and isotropic cell aggregate self-organized into a spherical shell structure surrounding a small cavity (lumen) (Fig. 1e, Day 3, Supplementary Fig. S2). Each organoid contained a single orseveral lumens.

PEG Coating. A ~10-µm-thick polyethylene glycol (PEG) hydrogel can be assembled on the glass cover slip to exclude surface adhesion or control surface stiffness[52]. Glass slides were plasma treated (1 min, 100W, 1 bar argon, 2 bar oxygen), and immediately coated with TMSMA solution (10 ml ethanol, 300 µL 1:10 glacial acetic acid:ddw, and 0.5 ml 3-(trimethoxysilyl) propyl methacrylate; Sigma, 440159), incubated for 1 h, double rinsed with ethanol, dried with nitrogen and stored in the dark. For the PEG mixture: photoinitiator stock solution was prepared as 100 mg 2,2-Dimethoxy-2-phenylacetophenone (Sigma, 196118) to 1ml 70% ethanol. PEG solution was prepared as 200 mg PEG-6000 diacrylate (Sigma, 701963) to 1ml PBS. The photoinitiator was mixed into the PEG solution to a final 0.1% concentration and stored at 4 °C. For gel curing: A 2.5 µL drop of PEG mixture was placed on the surface-treated slide, and carefully closed from the top with a 18-mm-diameter circular coverslip. The PEG mixture uniformly spread between the two surfaces, thus reaching an average thickness of ~10 µm. The solution was cross-linked by exposure to UV light. The 18mm coverslip was removed gently using tweezers. The PEG-coated coverslip was washed and incubated over night with sterile PBS. Before device assembly the slide was dried with nitrogen, and the PEG gel was clearly visible as an opaque disc on the clear coverslip.

Lipidure coating. Glass slides and membrane-assembled Petri dish were coated with antiadhesive Lipidure-CM5206 (NOF Corporation) according to the manufacturer's protocol[53]. A 0.5 wt% solution was prepared by dissolving 0.05g Lipidure powder in 10 ml of ethanol. A ~200 µl Lipidure solution was placed on the coverslip/membrane surface for 1–2 min. The solution was aspirated. The process was repeated twice. The surfaces were dried with nitrogen followed by treatment in a 50 °C oven for 1 h.

Imaging and analysis. Imaging was carried out in a spinning disk confocal microscope based on an OLYMPUS IX83 inverted microscope, VisiScope CSU-W1-T1 confocal system (Visitron Systems, Germany) and an sCMOS 4.2 MPixel camera. Imaging was performed using the VisiView software. Image and data analysis were carried out in FIJI and Matlab 2016b.

Cell line and CRISPR genome editing. In this work, we used early passages of the NIH-approved embryonic stem cell line NIHhESC-10-0079 (WIBR3). Human ES cells were grown in optimal naive NHSM conditions (RSET—Stem Cell Technologies INC) as described elsewhere[51]. Three isogenic mutant cell-line clones were generated by partial deletion of the *LIS1* gene from one allele of the wild-type cell line. To insert the *LIS1* mutation we used the Clustered regularly interspaced short palindromic repeats (CRISPR) genome editing method. We used double Cas9 nickase to reduce the probability of off-target effects. The two guide-RNA sequences, GGACGGGGAATCCATTCTTTTGG and AATATGCATTGAGTGGTCACAGG, were designed according to http://crispr.mit.edu/, and targeted the fourth coding exon region of the *LIS1* gene. The corresponding oligonucleotides were cloned into a pX335 vector, which contains an expression vector for mutant Cas9 (nickase). Cells were transfected using electroporation. In addition to the plasmid encoding the gRNA and Cas9, tracer amounts of a GFP expression vector were added. Three days after transfection, the cells were subject to fluorescence-activated cell sorting (FACS) and plated at a density of 2,000 cells per plate, allowing for the growth of single-cell-derived colonies. Colonies were picked, and screened by RNA and protein levels. Since *LIS1* knock-outs are embryonic lethal we expected only *LIS1* +/− heterozygous deletions[54]. Three *LIS1* +/− clones were used in the study: 10F, 9G and 45, respectively referred to as clones 1,2 and 3 in the main text. Reduced LIS1 protein levels were verified by western blot (Supplementary Fig. S15). Cell lines were regularly checked for mycoplasma contamination. Spectral karyotyping test was performed to cell lines WIBR3 (100% normal metaphases, $N=10$), and *LIS*, +/−10F (12 normal metaphases, 1 metaphase with chromosome 17 duplication, total $N=13$).

Cell electroporation and fluorescence reporters. Human embryonic stem cells were stably labelled with a fluorescent H2B-mCherry reporter, labelling chromosomes, and a Lifeact-GFP reporter labelling actin. Cell transfection was carried out in a NEPA21 electroporation system according to the company protocol (Nepa Gene, Japan). To ensure stable expression over the whole cell lineage we used the PiggyBac transposase method, which allows DNA integration into the cell genome at random sites[55,56]. We co-electroporated pCAG:H2B-mCherry and pCAG:LiveAct-GFP plasmids together with a pCAG-PBase plasmid expressing the PiggyBac transposase. The reporter plasmids carried inverted terminal repeat sequences (ITRs), recognized by PiggyBac transposase, before and after the promoter:gene sequence. Following electroporation, cells were plated, passaged once after several days, and selected using FACS.

AFM sample preparation. Atomic force microscopy (AFM) experiments were carried out on cells cultured on 5-cm-diameter tissue culture dishes. Cells were cultured in two conditions: either as embryonic stem cell colonies (ES)[51] or differentiated to neuronal progenitors (NP) as described[57]. For the ES sample, ES cells were plated onto a Matrigel-coated plate, cultured for about a week in NHSM media (Supplementary Table S1) and taken for AFM analysis. For the NP sample, ES cells were plated onto a 10-cm-diameter plate coated with Matrigel, cultured until they reached confluency, and then transferred to a 5-cm-diameter plate. After 24 h, the NHSM media was replaced with Neuronal Differentiation media (Supplementary Table S1) supplemented with TGFB inhibitor (SB431542, 5 µM), Noggin (0.5 µg ml^{-1}) and Vitamin A (present in B27 supplement, Supplementary Table S1). Cells were cultured for 14 days, with daily media exchange, and were taken for AFM analysis.

AFM experiments. AFM studies were performed using a JPK Nanowizard 3 and Nanosensors qp-BioAC probes (probe 1, force constant of approximately 50 pN nm^{-1}) in QI mode. This mode allows acquisition of topographic images simultaneously with mechanical data (for example, stiffness and adhesion). It also allows collection of force–distance curves at each pixel which can subsequently be converted to elastic modulus after calibration of the optical lever sensitivity and cantilever spring constant, by applying a contact mechanical model. Initially, regions of approximately $20\times20\,\mu m^2$ were scanned at moderate resolution to locate the positions of the cells and their boundaries. Then, zoomed areas centred on selected cells were acquired, approximately $5\times5\,\mu m^2$ at 32×32 pixels, together with the pixel-resolved force curves. Ultimate force and pull-back distance were tuned to ensure penetration into the cell of nominally 300–800 nm and complete disengagement from the cell for each cycle. The tip approached the surface at a speed of 50 µm s^{-1}. The traces showed no evidence of significant adhesion, had good repeatability in a single location, and were analysed using a Herzian model

presuming a Poisson ratio of 0.5 and a conical probe with an opening half-angle of 20 degrees. For analysis, force curves from the cell were selected using the maps, avoiding cell–cell border regions. Several thousand force curves were combined from 7–10 different cells for the analysis of each cell line (Fig. 5k, Supplementary Figs. S19,20).

Cytoskeleton drug experiments. Cytoskeleton drug experiments were carried out directly in the organoid device. For the long-term experiments (Figs. 4a,b), 5 μM blebbistatin was added during days 6–10 after Matrigel embedding. In the short-term experiments (Fig. 4c–e), drugs were added to the media, and the organoids were incubated for 3 hours in a cell incubator. Organoids were imaged before and after the addition of the drugs. Drugs were used at the following concentrations: Rock Inhibitor (Y-27632) 20 μM, blebbistatin 50 μM and nocodazole 10 μM.

Laser microdissection experiments. Laser microdissection experiments were carried out directly on the organoid device, using the Palm MicroBeam Zeiss system. The system works with a pulsed 337 nm UV Nitrogen Laser. The irradiation area was chosen using Lifeact fluorescence imaging with a 10× objective (Supplementary Fig. S14, green line). Laser irradiation was performed using a 40× air objective, in Laser Pressure Catapulting (LPC) mode. In this mode, the laser pulses are localized in discrete locations within the irradiation area (Supplementary Fig. S14, blue dots). The following parameters were used: 60% power, 100% focus, and speed 1. The organoids were fluorescently imaged before and after the laser microdissection, which lasted about a minute.

Immunostaining. Immunostaining was carried out directly in the organoid device. Organoids were fixed with PFA 2.5% for two hours, washed three times in PBS and permeabilized using PBS-Triton 0.1% for 15 min, followed by 30 min blocking (30% Horse serum, 10% Fetal Calf Serum, 0.1% Triton X-100 in PBS). The organoids were incubated for two hours of primary antibody diluted in blocking solution (Rabbit anti-PAX6 1:200 Covance PRB-278P, Mouse anti-NeuN 1:200 MILLIPORE mab377), washed in PBS, incubated for twenty minutes with secondary antibody 1:200 in blocking, followed by incubation with 4′,6-diamidino-2-phenylindole (DAPI) for 10 min and PBS washing. Organoid devices were imaged following the immunostaining.

Contour analysis of human brains. Contour analysis of a healthy human brain (Fig. 5i, inset) was done on a single post-mortem section image (Brain Biodiversity Bank, Michigan State University, https://msu.edu/~brains/, coronal section #2000). Analysis of lissencephalic brain was done on a patient MRI scan image (courtesy of Dr. Nadia Bahi-Buisson, French Institute of Health and Medical Research).

Bulk RNA-seq library construction and sequencing. Total RNA from was extracted using the RNeasy Mini kit (Qiagen) under the manufacturer's protocols. RNA was extracted at three time points: as human embryonic stem cells, and as organoids 5 and 12 days after Matrigel embedment. Three repeats were taken for each time point. Organoid RNA was extracted directly from the device, with a total of 20 to 40 organoids for each repeat. RNA concentration and integrity were measured using Nanodrop (Thermo Scientific) and an Agilent Tapestation, respectively. Libraries were prepared from 50 ng of total RNA using Bulk MARS-seq, a modified version of directional gene expression through the 3′ end developed for single-cell RNA-seq (MARS seq), to produce expression libraries[58]. The quality of the libraries was assessed by TapeStation and qPCR, and high-quality libraries were sequenced by the Illumina NextSeq 500 sequencer to obtain a single read of 75bp.

Transcriptome assembly and analysis. Raw data files were processed by removing the adapters from the raw sequencing reads using Cutadapt[59] after quality assessment of FASTQ files using the FastQC tool[60]. Reads were then aligned to the reference genome GRCh37/hg38 using STAR[61]. Differential expression was tested by fitting raw counts on a negative binomial distribution using DESeq2[62]. Genes were sorted according to their log2-transformed fold-change values after shrinkage in DESeq2. The clusters of pathways that shared many leading-edge genes were detected using GeneAnalytics[63], and then manually curated to elucidate the important phenotype-associated pathway groups visualized on the heatmaps. Hierarchical clustering was performed using the R software. First, all the differentially expressed genes for a genotype and/or developmental time point were identified using the methods listed above, and clustering was subsequently performed using the *hclust* and *dendsort* package in R. Gene set enrichment analysis (GSEA) was carried out using the R package edgeR[64], and ROAST[65] function from the R package Limma (Supplementary Fig. S5). Differentially expressed genes were manually divided into radial glia and neuronal categories according to previous works[66–73] (Supplementary Fig. S6).

Data availability. The data that support the plots within this paper and other findings of this study are available from the corresponding author upon request. RNA sequencing data has been submitted to GEO (GSE106821).

References

51. Gafni, O. et al. Derivation of novel human ground state naive pluripotent stem cells. *Nature* **504**, 282–286 (2013).
52. Cuchiara, M. P., Allen, A. C. B., Chen, T. M., Miller, J. S. & West, J. L. Multilayer microfluidic PEGDA hydrogels. *Biomaterials* **31**, 5491–5497 (2010).
53. Kim, J.-Y. et al. 3D spherical microtissues and microfluidic technology for multi-tissue experiments and analysis. *J. Biotechnol.* **205**, 24–35 (2015).
54. Hirotsune, S. et al. Graded reduction of Pafah1b1 (Lis1) activity results in neuronal migration defects and early embryonic lethality. *Nat. Genet.* **19**, 333–339 (1998).
55. Wu, S. C.-Y. et al. piggyBac is a flexible and highly active transposon as compared to sleeping beauty, Tol2, and Mos1 in mammalian cells. *Proc. Natl Acad. Sci. USA* **103**, 15008–15013 (2006).
56. Siddiqi, F. et al. Fate mapping by piggyBac transposase reveals that neocortical GLAST+ progenitors generate more astrocytes than Nestin+ progenitors in rat neocortex. *Cereb. Cortex.* **24**, 508–520 (2014).
57. Shi, Y., Kirwan, P., Smith, J., Robinson, H. P. C. & Livesey, F. J. Human cerebral cortex development from pluripotent stem cells to functional excitatory synapses. *Nat. Neurosci.* **15**, 477–486 (2012). S1.
58. Jaitin, D. A. et al. Massively parallel single-cell RNA-seq for marker-free decomposition of tissues into cell types. *Science* **343**, 776–779 (2014).
59. Martin, M. Cutadapt removes adapter sequences from high-throughput sequencing reads. *EMBnet. Journal.* **17**, 10 (2011).
60. S., A. FastQC: a quality control tool for high throughput sequence data. *Babraham Institute* http://www.bioinformatics.babraham.ac.uk/projects/fastqc (2010).
61. Dobin, A. et al. STAR: ultrafast universal RNA-seq aligner. *Bioinformatics* **29**, 15–21 (2013).
62. Love, M. I., Huber, W. & Anders, S. Moderated estimation of fold change and dispersion for RNA-seq data with DESeq2. *Genome Biol.* **15**, 550 (2014).
63. Ben-Ari Fuchs, S. et al. GeneAnalytics: An integrative gene set analysis tool for next generation sequencing, RNAseq and MicroarrayData. *OMICS* **20**, 139–151 (2016).
64. Robinson, M. D., McCarthy, D. J. & Smyth, G. K. edgeR: a Bioconductor package for differential expression analysis of digital gene expression data. *Bioinformatics* **26**, 139–140 (2010).
65. Wu, D. et al. ROAST: rotation gene set tests for complex microarray experiments. *Bioinformatics* **26**, 2176–2182 (2010).
66. Ma, T. et al. Subcortical origins of human and monkey neocortical interneurons. *Nat. Neurosci.* **16**, 1588–1597 (2013).
67. Lui, J. H. et al. Radial glia require PDGFD–PDGFRβ signalling in human but not mouse neocortex. *Nature* **515**, 264–268 (2014).
68. Liu, Y. et al. Medial ganglionic eminence-like cells derived from human embryonic stem cells correct learning and memory deficits. *Nat. Biotechnol.* **31**, 440–447 (2013).
69. Johnson, M. B. et al. Single-cell analysis reveals transcriptional heterogeneity of neural progenitors in human cortex. *Nat. Neurosci.* **18**, 637–646 (2015).
70. Close, J. L. et al. Single-cell profiling of an in vitro model of human interneuron development reveals temporal dynamics of cell type production and maturation. *Neuron* **93**, 1035–1048.e5 (2017).
71. Camp, J. G. et al. Human cerebral organoids recapitulate gene expression programs of fetal neocortex development. *Proc. Natl Acad. Sci. USA* **112**, 15672–15677 (2015).
72. Lancaster, M. A. et al. Guided self-organization and cortical plate formation in human brain organoids. *Nat. Biotechnol.* **35**, 659–666 (2017).
73. Onorati, M. et al. Molecular and functional definition of the developing human striatum. *Nat. Neurosci.* **17**, 1804–1815 (2014).